

Article

Deep-Learning-Based Automatic Segmentation of Parotid Gland on Computed Tomography Images

Merve Önder ¹, Cengiz Evli ¹, Ezgi Türk ², Orhan Kazan ³, İbrahim Şevki Bayraktar ^{4,5,6}, Özer Çelik ^{5,7}, Andre Luiz Ferreira Costa ⁸, João Pedro Perez Gomes ⁹, Celso Massahiro Ogawa ⁸, Rohan Jagtap ⁶ and Kaan Orhan ^{1,10,11,*}

¹ Department of Dentomaxillofacial Radiology, Faculty of Dentistry, Ankara University, Ankara 06000, Turkey

² Dentomaxillofacial Radiology, Oral and Dental Health Center, Hatay 31040, Turkey

³ Health Services Vocational School, Gazi University, Ankara 06560, Turkey

⁴ Department of Oral and Maxillofacial Radiology, Faculty of Dentistry, Eskisehir Osmangazi University, Eskisehir 26040, Turkey

⁵ Eskisehir Osmangazi University Center of Research and Application for Computer-Aided Diagnosis and Treatment in Health, Eskisehir 26040, Turkey

⁶ Division of Oral and Maxillofacial Radiology, Department of Care Planning and Restorative Sciences, University of Mississippi Medical Center School of Dentistry, Jackson, MS 39216, USA

⁷ Department of Mathematics-Computer, Faculty of Science, Eskisehir Osmangazi University, Eskisehir 26040, Turkey

⁸ Postgraduate Program in Dentistry, Cruzeiro do Sul University (UNICSUL), São Paulo 01506-000, SP, Brazil

⁹ Department of Stomatology, Division of General Pathology, School of Dentistry, University of São Paulo (USP), São Paulo 13560-970, SP, Brazil

¹⁰ Department of Dental and Maxillofacial Radiodiagnostics, Medical University of Lublin, 20-093 Lublin, Poland

¹¹ Ankara University Medical Design Application and Research Center (MEDITAM), Ankara 06000, Turkey

* Correspondence: call53@yahoo.com; Tel.: +48-81-448-50-00



Citation: Önder, M.; Evli, C.; Türk, E.; Kazan, O.; Bayraktar, İ.Ş.; Çelik, Ö.; Costa, A.L.F.; Gomes, J.P.P.; Ogawa, C.M.; Jagtap, R.; et al. Deep-Learning-Based Automatic Segmentation of Parotid Gland on Computed Tomography Images. *Diagnostics* **2023**, *13*, 581. <https://doi.org/10.3390/diagnostics13040581>

Academic Editors: Jaafar M. Alghazou and Ghazanfar Latif

Received: 10 December 2022

Revised: 23 January 2023

Accepted: 2 February 2023

Published: 4 February 2023



Copyright: © 2023 by the authors. Licensee MDPI, Basel, Switzerland. This article is an open access article distributed under the terms and conditions of the Creative Commons Attribution (CC BY) license (<https://creativecommons.org/licenses/by/4.0/>).

Abstract: This study aims to develop an algorithm for the automatic segmentation of the parotid gland on CT images of the head and neck using U-Net architecture and to evaluate the model's performance. In this retrospective study, a total of 30 anonymized CT volumes of the head and neck were sliced into 931 axial images of the parotid glands. Ground truth labeling was performed with the CranioCatch Annotation Tool (CranioCatch, Eskisehir, Turkey) by two oral and maxillofacial radiologists. The images were resized to 512 × 512 and split into training (80%), validation (10%), and testing (10%) subgroups. A deep convolutional neural network model was developed using U-net architecture. The automatic segmentation performance was evaluated in terms of the F1-score, precision, sensitivity, and the Area Under Curve (AUC) statistics. The threshold for a successful segmentation was determined by the intersection of over 50% of the pixels with the ground truth. The F1-score, precision, and sensitivity of the AI model in segmenting the parotid glands in the axial CT slices were found to be 1. The AUC value was 0.96. This study has shown that it is possible to use AI models based on deep learning to automatically segment the parotid gland on axial CT images.

Keywords: artificial intelligence; deep convolutional neural network; salivary glands; U-net; computed tomography

1. Introduction

Salivary glands are important exocrine organs of the human body, responsible for the production of saliva as well as various digestive enzymes. Human salivary glands are divided into major and minor glands according to their size and function. The major salivary glands are defined as the parotid, submandibular, and sublingual glands [1,2]. The parotid gland is the largest in size, responsible for producing 60 to 65% of the oral cavity's total saliva, and envelops the mandible's ramus [3,4]. The facial nerve subdivides the

parotid gland into superficial and deep lobes [5]. In 2017, the World Health Organization proposed a classification with more than 30 types of salivary gland tumors categorized as being either malignant or benign histological subtypes. Benign salivary gland tumors constitute approximately 6% of tumors diagnosed in the head and neck region [1,2]. Salivary gland tumors can originate from distinct types of glandular cells, and they exhibit considerable variances in their clinical, pathological, and biological characteristics. The current treatment options are multimodality therapy, chemotherapy, radiation therapy, and surgical resection [6]. The malignant or benign characteristics of the salivary gland tumor are important in terms of the prognosis and treatment options, since malignant tumors require a more invasive operation [7,8]. Improvements in salivary gland imaging, consistent with the histopathological findings, will contribute to the relevant clinical decision [9,10].

Several imaging techniques can be adopted to reveal the status of the parotid glands, each with its own advantages and limitations. The magnetic resonance imaging (MRI) and computed tomography (CT) techniques are the primary methods for evaluating the parotid gland anatomically, pathologically, and structurally, by enabling the cross-sectional evaluation of the salivary glands [11–13]. CT is proposed for cases where an inflammatory condition such as sialectasis, abscess, stone, and acute inflammation is suspected, and when MRI is contraindicated. Nevertheless, MRI is the preferred imaging technique in patients with a high suspicion of malignancy. In addition, ultrasonic imaging can be beneficial in pediatric and pregnant patients for an initial investigation, particularly in cases involving lesions of the parotid gland's superficial lobe [14].

Progress in digital imaging has paved the way for implementing various artificial intelligence (AI) tools for segmenting, detecting, and classifying the anatomical and pathological structures [15,16]. Currently, the practice of radiology benefits significantly from AI applications. Implementing such tools can be highly beneficial in removing the burden of performing certain tasks repeatedly including segmenting organs or nerves or for extracting the quantitative data that are more beneficial, thus enabling clinicians to increase their focus on attempting to solve complicated clinical issues [17,18]. Still, there are many problems, such as the need for large datasets and training, regulation issues, and medicolegal responsibility, which are suggested as barriers to the efficient application of AI in radiologists' normal practice. For the success of a developed AI model, the use of quality data in education and the correct labeling process are both important [19,20].

Image segmentation is the subject of various fields such as transportation, architecture, and medical imaging. Traditional segmentation methods, such as boundary extraction, threshold-based segmentation, and region-based segmentation can be adopted in manual segmentation of the medical images [21,22]. However, manual segmentation requires expertise and is a time-consuming process. In the deep learning approach, features are extracted by algorithms by establishing multilayered mathematical models. Thus, developers can benefit from the advantage of using big data in model training [22,23]. Convolutional neural network (CNN) algorithms have received attention for their success in image processing tasks. U-Net is an architecture developed for image segmentation. The basic structure consists of contraction and expansion paths, which are almost symmetrical, resulting in a u-like shape [21–23]. Deep learning can be utilized in U-Net algorithms, and its better performance than its competitors using a limited dataset makes this architecture popular in segmentation tasks in the medical field where data are limited [21].

Recently, the deep learning method has been utilized extensively, especially in medical image processing where segmentation is needed [16,24]. Segmentation from head and neck CT images has been performed with the deep learning method [25,26]. In 2014, Yang et al. proposed a system based on atlas registration and a support vector machine model for automated segmentation of the parotid gland using MR images. Fifteen patients with head and neck radiotherapy (42 MRI data) were included, and the difference between the model and the human tracings was reported as 7.98% and 8.12% for the left and the right parotid, respectively [27]. In 2018, Močnik et al. developed an automatic multimodal method for segmentation of the parotid glands from a CT and MRI pair of patient data.

Elastix and ANTs tools were employed to register the MRI image to the CT, and the CNN model was implemented using Microsoft Cognitive Toolkit. The researchers compared the results of the proposed multimodal model with the CT-only modality and reported a Dice overlapping coefficient of 78.8% for the first and 76.5% for the latter approach [28]. Hänsch et al. developed a U-Net based system for segmenting the parotid from CT images that were two-dimensional, three-dimensional, and in a two-dimensional ensemble mode, in 2019. In total, 254 head and neck CT scans from two different clinical sites were selected, and in addition to the models' performance for segmentation, the number of the training samples needed was also investigated. The authors reported a mean Dice similarity of 0.83 for all three models, and increasing the training cases to more than 250 did not increase the Dice coefficient significantly [29].

This study aims to develop a deep convolutional neural network (dCNN) algorithm based on U-Net architecture and to evaluate the model's performance in the automatic segmentation of the parotid glands on axial-CT images.

2. Materials and Methods

2.1. Study Design

A U-net based algorithm was developed using the Pytorch library for the automatic segmentation of the parotid gland in axial slices of head and neck CT images (CranioCatch, Eskisehir-Turkey). All procedures performed in studies involving human participants were in accordance with the ethical standards of the institutional and/or national research committee and with the 1964 Helsinki declaration and its later amendments or comparable ethical standards. The study protocol was approved by the Non-interventional Clinical Research Ethics Board of The University of Campinas (UNICAMP) with the decision number 79765917.5.0000.5404 (decision date 18 March 2018, meeting number 2.553.836).

2.2. Study Data

In this retrospective study, 30 anonymized CT datasets were selected from the archive of the Radiology Department of the Faculty of Medical Sciences, University of Campinas (UNICAMP). Samples with clearly visible parotid glands bilaterally were included, while images with a gross anomaly and artifacts on the parotid gland were excluded. Radiographic data were acquired by a 16-slice CT scanner (Siemens Somatom Sensation 16, Forchheim, Germany) with the constant parameters of 0.6 mm detector collimation, 120 kVp tube voltage, 0.6 s gantry rotation time, 1.5 mm reconstructed section thickness, and 1 mm reconstruction intervals. The patient data in three-axes (sagittal, coronal, and axial) were reconstructed into volumetric data and exported in Digital Imaging and Communication in Medicine (DICOM) file format. The resulting DICOM files were imported to Pydicom (<https://pydicom.github.io/datasets> (accessed on 1 June 2022)) software, and in total, 931 axial-CT images with a unilateral or bilateral appearance of the parotid gland were exported in Joint Photographic Experts Group (JPEG) format.

2.3. Ground Truth Labeling

The CranioCatch Annotation Tool (CranioCatch, Eskisehir, Turkey) was developed with polygonal box segmentation technique for labeling of the parotid glands on the axial CT images. The ground truth was determined by the consensus of two experts in oral and maxillofacial radiology (I.S.B. with 11 years' experience and M.O. with 2 years' experience).

2.4. Data Split

The 931 axial images were resized to 512×512 pixels. The dataset was separated into the training (80%), validation (10%), and testing (10%) groups randomly.

Training group: 745 (1445 labels);

Validation group: 93 (178 labels);

Testing group: 93 (184 labels).

2.5. Development of the U-Net Based dCNN Model

The U-net based automated parotid segmentation algorithm was developed in the Python environment (v.3.6.1; Python Software Foundation, Wilmington, DE, USA) using the PyTorch library. The model was trained for 700 epochs with learning rate of 0.00001. Mathematical processing in the model's training was performed with a Dell PowerEdge T640 Calculation Server (Dell Inc., Round Rock, TX, USA), Dell PowerEdge T640 GPU Calculation Server (Dell Inc., Round Rock, TX, USA), and a Dell PowerEdge R540 Storage Server (Dell Inc., Round Rock, TX, USA) in the Eskisehir University Dentistry Faculty Dental-AI Laboratory, (Appendix A), (Figure 1).

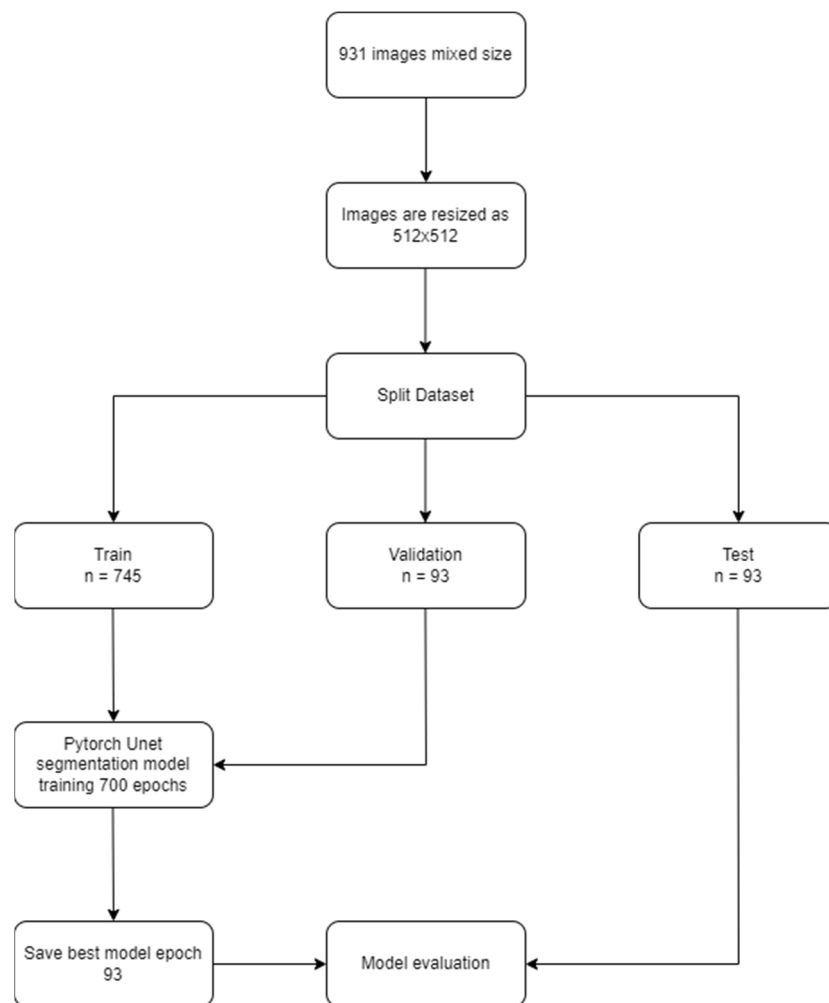


Figure 1. Model pipeline of parotid gland segmentation.

2.6. Statistics for the Model's Performance

The model's performance in the automated segmentation of the parotid glands on the axial CT images was evaluated with the F1-score, the precision, the sensitivity, and the area under curve (AUC) values. The model's result was considered successful if the prediction and the ground truth intersected by more than 50% in each individual image slice. The true positive (TP), false positive (FP), and false negative (FN) results were determined for calculating the performance metrics. The definitions and the formulas for calculating the model's performance are described below:

True positive (TP): At least 50% of the pixels intersect between the automatic segmentation algorithm and the ground truth;

False positive (FP): At least 50% of the pixels of the automatic segmentation algorithm do not intersect with the ground truth;

False negative (FN): At least 50% of the pixels of the ground truth do not intersect with the results of the automatic segmentation algorithm;

Sensitivity (Recall, True positive rate (TPR)) = $TP / (TP + FN)$;

Precision (Positive predictive value (PPV)) = $TP / (TP + FP)$;

F1-Score = $2TP / (2TP + FP + FN)$.

3. Results

The U-Net based algorithm (CranioCatch, Eskisehir-Turkey) predicted the pixels of the parotid glands with more than 50% intersection in all samples (Figure 2). The values of the F-measure, precision, and sensitivity were all determined to be 1.0 in terms of segmenting the parotid gland axial slices of CT images successfully (Table 1). The Area Under Curve (AUC) value was found to be 0.96 (Figures 3 and 4).

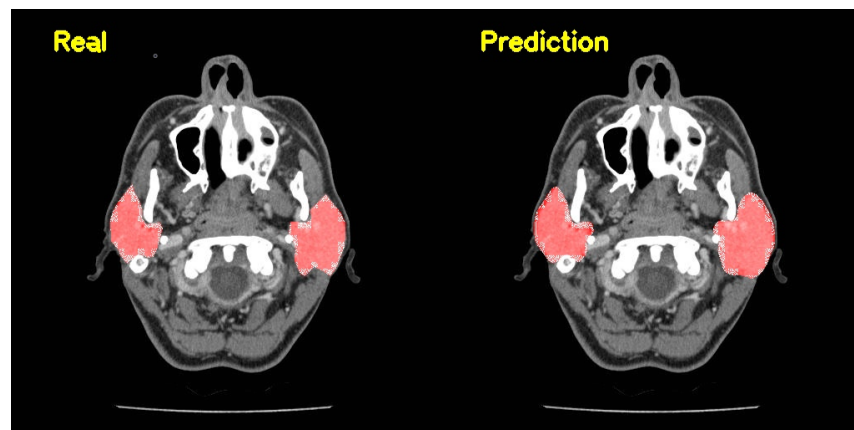


Figure 2. The automatic segmentation of the parotid gland utilizing the Artificial Intelligence model in axial CT slices.

Table 1. Results showing the predictive performance utilizing the AI model (CranioCatch, Eskisehir-Turkey) in terms of segmenting the parotid gland with the testing data.

Number	TP	FP	FN	Sensitivity	Precision	F1-Score
Sample	93	0	0	1.0	1.0	1.0
Label	184	0	0	1.0	1.0	1.0

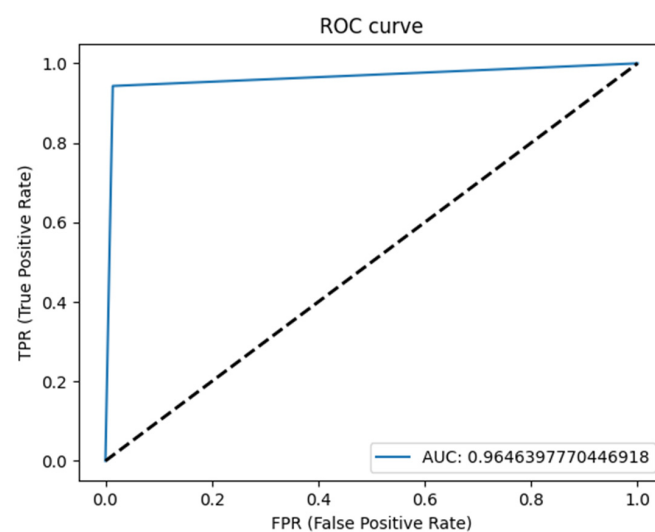


Figure 3. ROC curve.

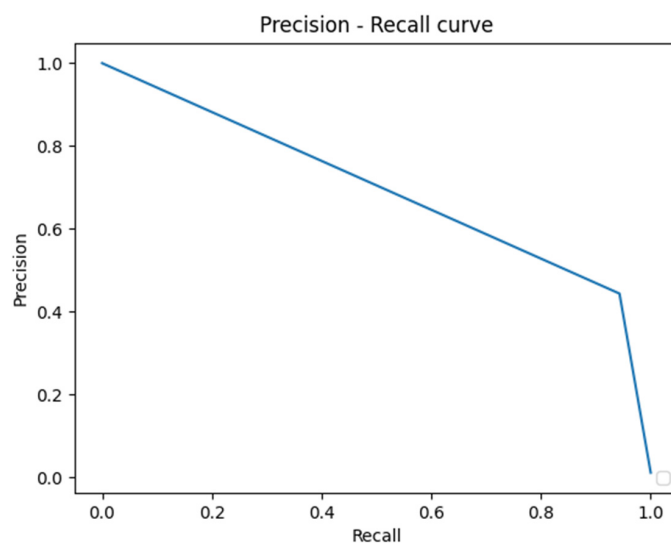


Figure 4. Precision–Recall curve.

4. Discussion

As new developments occur in terms of deep learning and neural techniques, artificial intelligence is being increasingly integrated into the field of medicine, and artificial intelligence has been used to solve clinical problems. Recently, at the same time as deep learning techniques are being used in the medical field, its application in dentistry has also increased. In the current study, the technique employed offers a comprehensive training approach to optimize the usage of datasets that have been partly annotated for the purpose of segmenting organs. Segmenting organs with precision and reliability can help to improve clinical applications including computer-aided detection, treatment, and surgical procedures. Organ segmentation also has the potential to be a critical factor in educating dental students [16,30,31]. Our study enables the segmentation of distinct IT images using a single network. To take advantage of the data from large scale datasets, previous researchers have adopted semi-supervised approaches in which the data were labeled weakly or potentially had no labels. This study is supplementary to previous approaches, and it is possible to amalgamate it with semi-supervised learning to assist with overcoming the issue of data need when segmenting organs. The findings of this study show that there were minimal differences in terms of the segmentation performance when training was performed on a large-scale dataset containing clinical quality references compared to a dataset that was smaller in size with curated quality references. In the future, an important additional step will involve the clinical qualitative assessment of the clinical admission of the contours that deep learning generates. It has been found the networks that are deeper with an increased number of parameters are also capable of consubstantiating a greater amount of data and facilitating additional improvements in the segmentation performance using additional samples. Furthermore, the performance of the deep learning techniques was more robust and had less variance compared to methods based on model- or atlas-based approaches with regard to the segmentation task. This could be due to the fact that the learned attributes could be representative of a broad anatomical diversity with no previous assumptions, and training may also have been conducted on a dataset with a larger size compared with the techniques used in the task [29,32].

In a study in which segmentations of five different internal organs were evaluated using the U-net algorithm in 2020, the accuracy values for these organs were determined to be 0.959, 0.813, 0.595, 0.900, and 0.911, respectively [33]. In our study, the accuracy value was found to be 1.0 for the parotid gland. A study conducted in 2016 focused on designing and training a 3D convolutional neural network for automatic detection of the liver, where the training dataset comprised 151 CT images, the validation dataset included 20 images, and the testing group included 10 images. In the results of this study, the average

accuracy value for the liver segmentation was found to be 97.6% [34]. Again, similar to our study, in a study using the U-net algorithm, CT images of COVID-19 patients were evaluated and the values for the sensitivity, precision, and F1-score were calculated as 0.8, 0.82 and 0.81, respectively. In the same study, it was shown that the results could be further improved by adding various modules to the U-net algorithm [35]. In another study using a fully connected network, which is a somewhat similar method, photographs of skin lesions were evaluated, and the F1-score and sensitivity values were found to be 0.912 and 0.918, respectively [36]. In another study performed with CT images of individuals diagnosed with COVID-19, the sensitivity and F1-score values were found to be 0.439 and 0.534, respectively, unlike our study and other similar studies [37]. In a study conducted in 2021 comparing human and CNN-based diagnosis, 855 CT images were used for training and validation and 256 true-positive, 279 false-positive, and 114 false-negative results were obtained. Based on these values, the sensitivity, precision, and F1-score values were calculated to be 0.691, 0.478, and 0.565, respectively [38]. In another study using the U-Net framework, fully automatic segmentation of the computer-aided planning of orthognathic surgery orthognathic surgery planning was performed on CT images. In this research, the number of CT images totaled 454, which were separated into cohorts for training/ validation ($n = 300$) and testing ($n = 153$). The Mean volumetric Dice Similarity Coefficient (vDSC) and surface Dice Similarity Coefficient at 1 mm (sDSC) were calculated for the test cohort, with values of 0.96 and 0.97 reported for the upper skull, 0.94 and 0.98 for the mandible, 0.95 and 0.99 for the upper teeth, 0.94 and 0.99 for the lower teeth, and 0.82 and 0.98 for the mandibular canal. Industry expert segmentation approval rates for the mandible, mandibular canal, upper skull, upper teeth and lower teeth were determined to be 93%, 89%, 82%, 69%, and 58%, respectively [39]. In another study that used a deep learning model based on a regression neural network to fully automate the process of segmenting airways using CBCT, 315 patient images were included. In this study, the analysis focused on the distinctions among the data measured using a manual process and data obtained via deep learning. Through the application of agreement analysis, the extraction of 61 samples was performed and then a comparison was made between the value obtained from the manual measurements and the value predicted by the deep learning network with respect to both coordinates and volumes. The intraclass correlation coefficient (ICC) that had the highest correlation was the total volume in the oropharynx (0.986), along with the hypopharynx (0.964), as well as the nasopharynx (0.912). The coordinate CV2(x) had the intraclass correlation coefficient (ICC) with the greatest correlation (0.963), whereas the lowest correlation was observed at CV4(y) (0.868) [40]. A comparison was made between the overall volume evaluated via deep learning and the measurements of the volume conducted utilizing regression analysis manually; the findings mirrored those of the current study in that the two measurements had slopes near to 1. In another study of orthognathic surgery patients using 160 whole skull CBCT scans (70 scans taken preoperatively and 90 taken postoperatively) using the 3D U-net algorithm of artificial intelligence, the mandible was segmented semi-automatically and fully automatically. On average, the time taken by the semi-automatic (SA) was 1218.4 s, while the time taken by the refined artificial intelligence (RAI) decreased significantly ($p < 0.0001$) to 456.5 s (2.7-fold decrease). According to the assessments of both inter- and intraoperator consistency, the performance of the RAI was superior to the SA for each of the metrics, suggesting that it was more consistent. Where the SA was taken as the ground truth, the intersection over union (IoU) score for the AI and RAI was 94.6% and 94.4%, respectively [41]. In our study, the automated parotid segmentation model was developed using U-Net architecture and deep learning techniques. The results of this study support that implementing such a system containing and not containing further user enhancements can maximize the efficiency, reduce human error, and provide more accurate predictions. In another retrospective study involving the segmentation of organs that utilized the U-Net AI algorithm, sample data were taken from individuals who had undergone a prostate MRI and ultrasound-MRI fusion transrectal biopsy in the period from September 2014 to

December 2016. Two experts in abdominal radiology segmented axial T2-weighted images manually, which subsequently acted as the ground truth. Subsequent to the process of manual segmentation, the images were employed for training on a customized hybrid 3D-2D U-Net CNN architecture in a fivefold cross-validation paradigm for neural network training and validation. Statistical analysis was performed based on the Dice score, which measures the extent to which the segmentations performed manually and those derived automatically overlap, as well as the Pearson linear correlation coefficient of the prostate volume. A total of 299 MRI exams involving 298 patients were used to train the CNN (overall amount of MR images = 7774). The mean Dice score of the customized hybrid 3D-2D U-Net was 0.898 (range, 0.890–0.908), while the prostate volume had a Pearson correlation coefficient of 0.974 [42]. Similar to our study, this research showed that the 3D-2D U-Net CNN performed highly effectively in prostate segmentation and volumetric assessment application. Compared to the abovementioned studies, it can be thought that there are two main reasons why the values in our study were more positive. First, it can be considered that the parotid gland borders were easier to detect when compared to other structures. Secondly, it is possible that the repetitive checks during segmentation helped us to obtain more successful training data.

5. Conclusions

The findings of this study demonstrated that it is possible to use AI models based on deep learning to automatically segment the parotid gland on the axial CT images. Despite all these positive results, new studies with a significantly higher amount of training data and larger ROIs are required to distinguish the parotid gland from other anatomical structures.

Author Contributions: Conceptualization, İ.Ş.B. and K.O.; Methodology, İ.Ş.B. and Ö.Ç.; Software, Ö.Ç.; Validation, İ.Ş.B., K.O. and Ö.Ç.; Formal Analysis, İ.Ş.B., K.O. and Ö.Ç.; Investigation, E.T., O.K. and R.J.; Resources, A.L.F.C., J.P.P.G. and C.M.O.; Data Curation, M.Ö., İ.Ş.B. and Ö.Ç.; Writing—Original Draft Preparation, M.Ö., C.E. and E.T.; Writing—Review and Editing, M.Ö., C.E. and K.O.; Visualization, İ.Ş.B.; Supervision, İ.Ş.B. and K.O.; Project Administration, İ.Ş.B., O.K., K.O. and Ö.Ç.; Funding Acquisition, İ.Ş.B. All authors have read and agreed to the published version of the manuscript.

Funding: This study received support from the Eskisehir Osmangazi University Scientific Research Projects Coordination Unit under grant number 202045E06.

Institutional Review Board Statement: All procedures adopted adhered to the ethical standards of the responsible committee on human experimentation (institutional and national) as well as the Helsinki Declaration of 1975, as revised in 2008.

Informed Consent Statement: Informed consent was acquired from all patients enrolled in the research.

Data Availability Statement: Not applicable.

Acknowledgments: We would like to thank Hakan Amasya for his support in the preparation of manuscript.

Conflicts of Interest: The authors declare that they have no conflicts of interest. The funders had no role in the design of the study; in the collection, analyses, or interpretation of data; in the writing of the manuscript; or in the decision to publish the results.

Appendix A

The Eskisehir Osmangazi University Faculty of Dentistry Dental-Artificial Intelligence (AI) Laboratory has advanced technology computer equipment, including a Dell PowerEdge T640 Calculation Server (Intel Xeon Gold 5218 2.3G, 16C/32T, 10.4GT/s, 22M Cache, Turbo, HT (125W) DDR4-2666, 32GB RDIMM, 3200MT/s, Dual Rank, PERC H330+ RAID Controller, 480GB SSD SATA Read Intensive 6Gbps 512 2.5in Hot-plug AG Drive), a PowerEdge T640 GPU Calculation Server (Intel Xeon Gold 5218 2.3G, 16C/32T, 10.4GT/s, 22M Cache, Turbo, HT (125W) DDR4-2666 2, 32GB RDIMM, 3200MT/s, Dual Rank, PERC H330+ RAID Controller, 480GB SSD SATA Read Intensive 6Gbps 512 2.5in Hot-plug AG

Drive, NVIDIA Tesla V100 16G Passive GPU), a PowerEdge R540 Storage Server (Intel Xeon Silver 4208 2.1G, 8C/16T, 9.6GT/s, 11M Cache, Turbo, HT (85W) DDR4-2400, 16GB RDIMM, 3200MT/s, Dual Rank, PERC H730P+ RAID Controller, 2Gb NV Cache, Adapter, Low Profile, 8TB 7.2K RPM SATA 6Gbps 512e 3.5in Hot-plug Hard Drive, 240GB SSD SATA Mixed Use 6Gbps 512e 2.5in Hot plug, 3.5in HYB CARR S4610 Drive), a Precision 3640 Tower CTO BASE workstation (Intel(R) Xeon(R) W-1250P (6 Core, 12M cache, base 4.1GHz, up to 4.8GHz) DDR4-2666, 64GB DDR4 (4 X16GB) 2666MHz UDIMM ECC Memory, 256GB SSD SATA, Nvidia Quadro P620, 2GB), and a Dell EMC Network Switch (N1148T-ON, L2, 48 ports RJ45 1GbE, 4 ports SFP+ 10GbE, Stacking).

References

1. Siegel, R.L.; Miller, K.D.; Jemal, A. Cancer statistics, 2019. *CA Cancer J. Clin.* **2019**, *69*, 7–34. [\[CrossRef\]](#)
2. Stenner, M.; Klussmann, J.P. Current update on established and novel biomarkers in salivary gland carcinoma pathology and the molecular pathways involved. *Eur. Arch. Otorhinolaryngol.* **2009**, *266*, 333–341. [\[CrossRef\]](#)
3. Mortazavi, H.; Baharvand, M.; Movahhedian, A.; Mohammadi, M.; Khodadoust, A. Xerostomia due to systemic disease: A review of 20 conditions and mechanisms. *Ann. Med. Health Sci. Res.* **2014**, *4*, 503–510. [\[CrossRef\]](#)
4. Dirix, P.; Nuyts, S. Evidence-based organ-sparing radiotherapy in head and neck cancer. *Lancet Oncol.* **2010**, *11*, 85–91. [\[CrossRef\]](#)
5. Lowe, L.H.; Stokes, L.S.; Johnson, J.E.; Heller, R.M.; Royal, S.A.; Wushensky, C.; Hernanz-Schulman, M. Swelling at the angle of the mandible: Imaging of the pediatric parotid gland and periparotid region. *Radiographics* **2001**, *21*, 1211–1227. [\[CrossRef\]](#)
6. Adelstein, D.J.; Koyfman, S.A.; El-Naggar, A.K.; Hanna, E.Y. Biology and management of salivary gland cancers. *Semin. Radiat. Oncol.* **2012**, *22*, 245–253. [\[CrossRef\]](#)
7. Lewis, A.G.; Tong, T.; Maghami, E. Diagnosis and Management of Malignant Salivary Gland Tumors of the Parotid Gland. *Otolaryngol. Clin. N. Am.* **2016**, *49*, 343–380. [\[CrossRef\]](#)
8. Stenner, M.; Molls, C.; Luers, J.C.; Beutner, D.; Klussmann, J.P.; Huettenbrink, K.B. Occurrence of lymph node metastasis in early-stage parotid gland cancer. *Eur. Arch. Otorhinolaryngol.* **2012**, *269*, 643–648. [\[CrossRef\]](#)
9. Yue, D.; Feng, W.; Ning, C.; Han, L.X.; YaHong, L. Myoepithelial carcinoma of the salivary gland: Pathologic and CT imaging characteristics (report of 10 cases and literature review). *Oral Surg. Oral Med. Oral Pathol. Oral Radiol.* **2017**, *123*, e182–e187. [\[CrossRef\]](#)
10. Kim, K.H.; Sung, M.-W.; Yun, J.B.; Han, M.H.; Baek, C.-H.; Chu, K.-C.; Kim, J.H.; Lee, K.-S. The significance of CT scan or MRI in the evaluation of salivary gland tumors. *Auris Nasus Larynx* **1998**, *25*, 397–402. [\[CrossRef\]](#)
11. Yousem, D.M.; Kraut, M.A.; Chalian, A.A. Major salivary gland imaging. *Radiology* **2000**, *216*, 19–29. [\[CrossRef\]](#)
12. Dong, Y.; Lei, G.W.; Wang, S.W.; Zheng, S.W.; Ge, Y.; Wei, F.C. Diagnostic value of CT perfusion imaging for parotid neoplasms. *Dentomaxillofac. Radiol.* **2014**, *43*, 20130237. [\[CrossRef\]](#)
13. Ginat, D.T.; Christoforidis, G. High-Resolution MRI Microscopy Coil Assessment of Parotid Masses. *Ear Nose Throat J.* **2019**, *98*, 562–565. [\[CrossRef\]](#)
14. Mikaszewski, B.; Markiet, K.; Smugała, A.; Stodulski, D.; Szurowska, E.; Stankiewicz, C. An algorithm for preoperative differential diagnostics of parotid tumours on the basis of their dynamic and diffusion-weighted magnetic resonance images: A retrospective analysis of 158 cases. *Folia Morphol.* **2018**, *77*, 29–35. [\[CrossRef\]](#)
15. Syeda-Mahmood, T. Role of Big Data and Machine Learning in Diagnostic Decision Support in Radiology. *J. Am. Coll. Radiol.* **2018**, *15*, 569–576. [\[CrossRef\]](#)
16. Litjens, G.; Kooi, T.; Bejnordi, B.E.; Setio, A.A.A.; Ciompi, F.; Ghafoorian, M.; van der Laak, J.A.W.M.; van Ginneken, B.; Sánchez, C.I. A survey on deep learning in medical image analysis. *Med. Image Anal.* **2017**, *42*, 60–88. [\[CrossRef\]](#)
17. Waymel, Q.; Badr, S.; Demondion, X.; Cotten, A.; Jacques, T. Impact of the rise of artificial intelligence in radiology: What do radiologists think? *Diagn. Interv. Imaging* **2019**, *100*, 327–336. [\[CrossRef\]](#)
18. (ESR) ESoR. What the radiologist should know about artificial intelligence—An ESR white paper. *Insights Imaging* **2019**, *10*, 44. [\[CrossRef\]](#)
19. Gulshan, V.; Peng, L.; Coram, M.; Stumpe, M.C.; Wu, D.; Narayanaswamy, A.; Venugopalan, S.; Widner, K.; Madams, T.; Cuadros, J.; et al. Development and Validation of a Deep Learning Algorithm for Detection of Diabetic Retinopathy in Retinal Fundus Photographs. *JAMA* **2016**, *316*, 2402–2410. [\[CrossRef\]](#)
20. Ravi, D.; Wong, C.; Deligianni, F.; Berthelot, M.; Andreu-Perez, J.; Lo, B.; Yang, G.-Z. Deep Learning for Health Informatics. *IEEE J. Biomed. Health Inform.* **2017**, *21*, 4–21. [\[CrossRef\]](#)
21. Du, G.; Cao, X.; Liang, J.; Chen, X.; Zhan, Y. Medical image segmentation based on u-net: A review. *J. Imaging Sci. Technol.* **2020**, *64*, 1–12. [\[CrossRef\]](#)
22. Siddique, N.; Paheding, S.; Elkin, C.P.; Devabhaktuni, V. U-net and its variants for medical image segmentation: A review of theory and applications. *IEEE Access* **2021**, *9*, 82031–82057. [\[CrossRef\]](#)
23. Azad, R.; Aghdam, E.K.; Rauland, A.; Jia, Y.; Avval, A.H.; Bozorgpour, A.; Karimijafarbigloo, S.; Cohen, J.P.; Adeli, E.; Merhof, D. Medical image segmentation review: The success of u-net. *arXiv* **2022**, arXiv:221114830.
24. Shen, D.; Wu, G.; Suk, H.I. Deep Learning in Medical Image Analysis. *Annu. Rev. Biomed. Eng.* **2017**, *19*, 221–248. [\[CrossRef\]](#)

25. Fritscher, K.; Raudaschl, P.; Zaffino, P.; Spadea, M.F.; Sharp, G.C.; Schubert, R. Deep neural networks for fast segmentation of 3D medical images. In Proceedings of the International Conference on Medical Image Computing and Computer-Assisted Intervention, Athens, Greece, 17–21 October 2016; Springer: Berlin/Heidelberg, Germany, 2016; pp. 158–165. [\[CrossRef\]](#)
26. Ibragimov, B.; Xing, L. Segmentation of organs-at-risks in head and neck CT images using convolutional neural networks. *Med. Phys.* **2017**, *44*, 547–557. [\[CrossRef\]](#)
27. Yang, X.; Wu, N.; Cheng, G.; Zhou, Z.; Yu, D.S.; Beitler, J.J.; Curran, W.J.; Liu, T. Automated segmentation of the parotid gland based on atlas registration and machine learning: A longitudinal MRI study in head-and-neck radiation therapy. *Int. J. Radiat. Oncol.* **2014**, *90*, 1225–1233. [\[CrossRef\]](#)
28. Močnik, D.; Ibragimov, B.; Xing, L.; Strojjan, P.; Likar, B.; Pernuš, F.; Vrtovec, T. Segmentation of parotid glands from registered CT and MR images. *Phys. Med.* **2018**, *52*, 33–41. [\[CrossRef\]](#)
29. Hänsch, A.; Schwier, M.; Gass, T.; Morgas, T.; Haas, B.; Dicken, V.; Meine, H.; Klein, J.; Hahn, H.K. Evaluation of deep learning methods for parotid gland segmentation from CT images. *J. Med. Imaging* **2019**, *6*, 011005. [\[CrossRef\]](#)
30. Shan, T.; Tay, F.R.; Gu, L. Application of Artificial Intelligence in Dentistry. *J. Dent. Res.* **2021**, *100*, 232–244. [\[CrossRef\]](#)
31. Carrillo-Perez, F.; Pecho, O.E.; Msc, J.C.M.; Paravina, R.D.; Della Bona, A.; Ghinea, R.; Pulgar, R.; Pérez, M.D.M.; Herrera, L.J.; Msc, F.C.-P.; et al. Applications of artificial intelligence in dentistry: A comprehensive review. *J. Esthet. Restor. Dent.* **2022**, *34*, 259–280. [\[CrossRef\]](#)
32. Raudaschl, P.F.; Zaffino, P.; Sharp, G.C.; Spadea, M.F.; Chen, A.; Dawant, B.M.; Albrecht, T.; Gass, T.; Langguth, C.; Lüthi, M.; et al. Evaluation of segmentation methods on head and neck CT: Auto-segmentation challenge 2015. *Med. Phys.* **2017**, *44*, 2020–2036. [\[CrossRef\]](#)
33. Kim, H.; Jung, J.; Kim, J.; Cho, B.; Kwak, J.; Jang, J.Y.; Lee, S.-W.; Lee, J.-G.; Yoon, S.M. Abdominal multi-organ auto-segmentation using 3D-patch-based deep convolutional neural network. *Sci. Rep.* **2020**, *10*, 6204. [\[CrossRef\]](#)
34. Hu, P.; Wu, F.; Peng, J.; Liang, P.; Kong, D. Automatic 3D liver segmentation based on deep learning and globally optimized surface evolution. *Phys. Med. Biol.* **2016**, *61*, 8676–8698. [\[CrossRef\]](#)
35. Raj, A.N.J.; Zhu, H.; Khan, A.; Zhuang, Z.; Yang, Z.; Mahesh, V.G.V.; Karthik, G. ADID-UNET-a segmentation model for COVID-19 infection from lung CT scans. *PeerJ Comput. Sci.* **2021**, *7*, e349. [\[CrossRef\]](#)
36. Yuan, Y.; Chao, M.; Lo, Y. Automatic Skin Lesion Segmentation Using Deep Fully Convolutional Networks with Jaccard Distance. *IEEE Trans. Med. Imaging* **2017**, *36*, 1876–1886. [\[CrossRef\]](#)
37. Elharrouss, O.; Subramanian, N.; Al-Maadeed, S. An Encoder-Decoder-Based Method for Segmentation of COVID-19 Lung Infection in CT Images. *SN Comput. Sci.* **2022**, *3*, 13. [\[CrossRef\]](#)
38. Schultheiss, M.; Schmette, P.; Boddien, J.; Aichele, J.; Müller-Leisse, C.; Gassert, F.G.; Gassert, F.T.; Gawlitza, J.F.; Hofmann, F.C.; Sasse, D.; et al. Lung nodule detection in chest X-rays using synthetic ground-truth data comparing CNN-based diagnosis to human performance. *Sci. Rep.* **2021**, *11*, 15857. [\[CrossRef\]](#)
39. Dot, G.; Schouman, T.; Dubois, G.; Rouch, P.; Gajny, L. Fully automatic segmentation of craniomaxillofacial CT scans for computer-assisted orthognathic surgery planning using the nnU-Net framework. *Eur. Radiol.* **2022**, *32*, 3639–3648. [\[CrossRef\]](#)
40. Park, J.; Hwang, J.; Ryu, J.; Nam, I.; Kim, S.-A.; Cho, B.-H.; Shin, S.-H.; Lee, J.-Y. Deep learning based airway segmentation using key point prediction. *Appl. Sci.* **2021**, *11*, 3501. [\[CrossRef\]](#)
41. Verhelst, P.-J.; Smolders, A.; Beznik, T.; Meewis, J.; Vandemeulebroucke, A.; Shaheen, E.; Van Gerven, A.; Willems, H.; Politis, C.; Jacobs, R. Layered deep learning for automatic mandibular segmentation in cone-beam computed tomography. *J. Dent.* **2021**, *114*, 103786. [\[CrossRef\]](#)
42. Ushinsky, A.; Bardis, M.; Glavis-Bloom, J.; Uchio, E.; Chantaduly, C.; Nguyentat, M.; Chow, D.; Chang, P.; Houshyar, R. A 3D-2D Hybrid U-Net Convolutional Neural Network Approach to Prostate Organ Segmentation of Multiparametric MRI. *AJR Am. J. Roentgenol.* **2021**, *216*, 111–116. [\[CrossRef\]](#) [\[PubMed\]](#)

Disclaimer/Publisher’s Note: The statements, opinions and data contained in all publications are solely those of the individual author(s) and contributor(s) and not of MDPI and/or the editor(s). MDPI and/or the editor(s) disclaim responsibility for any injury to people or property resulting from any ideas, methods, instructions or products referred to in the content.